Solar driven photocatalytic disinfection by Z-scheme heterojunction of In$_2$O$_3$/g-C$_3$N$_4$: Performance, mechanism and application

Xiongjian Chen [a], Yanchao Jin [a,e,*], Peiwen Huang [a], Zhanwang Zheng [b], Li-Ping Li [c], Chun-Yan Lin [d], Xiao Chen [a,e], Rui Ding [a,e], Jianxi Liu [a,e], Riyao Chen [a,e,*]

[a] College of Environmental and Resource Sciences, Fujian Normal University, Fuzhou 350117, Fujian, China
[b] Zhejiang Sunda Public Environmental Protection Co., Ltd., Hangzhou 310012, China
[c] Research and Development Center for Watershed Environmental Eco-Engineering, Beijing Normal University, Zhuhai 519087, China
[d] School of Materials and Chemical Engineering, Minjiang University, Fuzhou 350108, Fujian, China
[e] Fujian Key Laboratory of Pollution Control & Resource Reuse, Fuzhou 350117, China

ABSTRACT

To realize an efficient solar disinfection, Z-scheme In$_2$O$_3$/g-C$_3$N$_4$ heterojunctions were prepared and its performances were investigated. The In$_2$O$_3$/g-C$_3$N$_4$ exhibits a wide light response range and a low carrier recombination rate. Due to the transfer of electron (e$^-$) and hole (h$^+$) between In$_2$O$_3$ and g-C$_3$N$_4$, the generations of superoxide (O$_2^{\bullet-}$) and hydroxyl radicals (HO$^\bullet$) were enhanced. O2• $-$' HO$^\bullet$ and h$^+$ played important roles for disinfection. Approximately 10^6 CFU/mL *E. coli* were inactivated within 90 min. In addition to cell membrane lysis, DNA was degraded. In$_2$O$_3$/g-C$_3$N$_4$ still revealed high sterilization efficiencies under natural sunlight or for actual wastewater treatment. Although humic acid and inorganic anions (Cl$^-$ < NO$_3^-$ < SO$_4^{2-}$ < H$_2$PO$_4^-$ < HCO$_3^-$) inhibited the disinfection, detection limit (DL, about 5.8-log removal) can be achieved. Furthermore, DL still could be achieved and the In$_2$O$_3$/g-C$_3$N$_4$ structure remained intact after 5 cycles. This study provides novel guidance for solar-driven water purification.

1. Introduction

According to the World Health Organization, drinking microbially contaminated water causes approximately 829,000 deaths each year [1]. Access to safe water is a key measure to prevent not only diarrheal diseases, but also acute respiratory infections and numerous neglected tropical diseases [2]. Currently, various efforts have been developed for water disinfection, including traditional chemical methods (chlorine, chlorine dioxide, ozone, alcohol and hydrogen peroxide) and ultraviolet irradiation (UV-A, UV-B and UV-C) [3]. However, some drawbacks are associated with such methods, such as the formation of mutagenic and carcinogenic disinfection by-products (DBPs) and high operational costs [4]. Consequently, it is vital to develop green, effective, low-cost sterilization techniques for drinking water treatment [5–7].

Recently, solar photocatalytic disinfection has been favored by researchers due to its advantages of environmental friendliness, energy saving and low cost [8–10]. Under sunlight irradiation, electrons (e$^-$) in the valence band (VB) of the photocatalyst can be excited into the conduction band (CB) [11]. Photogenerated holes (h$^+$) and electrons

(e$^-$) participate in redox reactions to generate reactive species (RS) [12]. As is well known, RS can cause cellular inactivation by cleaving cell membranes and degrading cytogenetic material [6,13]. Because of the unique chemical stability and tunable electronic band structure properties, graphite carbon nitride (g-C$_3$N$_4$) has recently garnered significant attention [14]. Compared with TiO$_2$, g-C$_3$N$_4$ has a narrower band gap energy, which makes it more suitable for visible-light-driven photocatalysis [15]. Significantly, g-C$_3$N$_4$ can be synthesized from a variety of low-cost nitrogen-rich precursors (melamine, dicyandiamide, thiourea, urea) by simple thermos polymerization [16]. However, the utilization of visible light is severely impeded by the rapid recombination of photo-generated electron-hole pairs in g-C$_3$N$_4$, which poses a significant drawback to its application [17]. Hence, it is essential to suppress the recombination of electron-hole pairs to improve the photocatalytic disinfection efficiency of g-C$_3$N$_4$.

Constructing a heterojunction between two semiconductors has been confirmed as one of the most effective approaches to promote the spatial separation of electron-hole pairs [18]. Semiconductors with different Fermi energy (EF) levels, electrons tend to diffuse from semiconductor

with higher EF to that with lower EF, and a built-in electric field (ED) will be formed at the heterojunction interface [19]. Due to the presence of ED, photo-excited carriers are forced to move between the two semiconductors, thus avoiding carrier recombination [20]. Recently, non-toxic indium oxide (In_2O_3) has attracted significant interest due to its ease of morphological modulation and doping [21]. As a typical n-type semiconductor, In_2O_3 has excellent optical and electrical properties, which has been extensively applied in gas sensors, transparent conductive oxides, solar cells and photocatalysis [22]. However, pure In_2O_3 suffers from low solar energy utilization and fast carrier recombination, both of which are generally overcome by constructing heterojunctions with another semiconductor [23]. For instance, In_2O_3/Bi_4O_7 Z-scheme heterojunctions were prepared for the photocatalytic degradation of doxycycline hydrochloride [24]. Under visible light irradiation, 92.7% of the contaminants could be degraded within 2 h, $O_2 \bullet -$ and $HO^\bullet$ played the main roles. Shen et al. [25] prepared In_2O_3/Ag_2CO_3 S-scheme heterojunctions and found that ED-driven electron transfer from Ag_2CO_3 to In_2O_3, which effectively inhibited carrier recombination. Thus, constructing a heterojunction between g-C_3N_4 and In_2O_3 may effectively separate carriers and thus improve photocatalytic disinfection efficiency. While, no reports have been found regarding the use of In_2O_3/g-C_3N_4 on bacterial inactivation. Consequently, it is imperative to investigate the photocatalytic disinfection properties and elucidate the RSs generation pathways of In_2O_3/g-C_3N_4 heterojunctions, which can offer a novel strategy for photocatalytic disinfection.

In this work, a novel In_2O_3/g-C_3N_4 photocatalyst was prepared by thermal polycondensation and ball milling methods and used for photocatalytic disinfection for the first time. The surface morphology, chemical composition, optical and photoelectrochemical properties of the In_2O_3/g-C_3N_4 were characterized. The disinfection performance and mechanism of the photocatalyst were evaluated. The heterojunction type formed between In_2O_3 and g-C_3N_4 was reasonably proposed and the generation pathways of RSs were elucidated. Finally, the applicability of the In_2O_3/g-C_3N_4 is assessed.

2. Materials and methods

2.1. Chemical reagents

Melamine ($C_3H_6N_6$, 99%), Indium acetate (In($C_2H_3O_2$)$_3$, 99%), 4-hydroxy-2,2,6,6-tetramethylpiperidine-1-oxyl ($C_9H_{18}NO_2$, TEMPOL, 98%), 2,2,6,6-Tetramethylpiperidine ($C_9H_{18}N$, TEMP, 97%), 2,2,6,6-Tetramethyl-1-piperidinyloxy ($C_9H_{18}NO$, TEMPO, 98%), 5,5-Dimethyl-1-pyrroline N-oxide ($C_9H_{18}NO$, DMPO, 97%) were supplied by Macklin Biochemical Co., Ltd., Shanghai, China. L-Histidine ($C_6H_9N_3O_2$) was purchased from Sinopharm Chemical Reagent Company, China. Isopropyl alcohol ((CH_3)$_2$CHOH, 99.7%), Sodium oxalate ($Na_2C_2O_4$, SO, 99.8%) and Formaldehyde solution (HCHO, 37% ~ 40%) were obtained from Xilong Scientific Co., Ltd. Bacterial genomic DNA rapid extraction reagent was purchased from Yifeixue Biotechnology Co., Ltd., Nanjing, China. Loading Buffer and Marker for DNA electrophoresis were supplied by Yogong Biolabs Co., Ltd. All solutions were prepared using deionized water, which was obtained from a Laboratory Water Purification System (Hitech Instruments Co., Ltd. Shanghai, China.).

2.2. Synthesis of photocatalysts

2.2.1. Synthesis of g-C_3N_4

The melamine was heated in a muffle furnace to obtain bulk g-C_3N_4. Typically, a certain amount of melamine was added to a covered alumina crucible and heated to 500 °C at 10 °C/min and retained for 2 h. Heating was then continued at 5 °C/min to 550 °C and retained for 1 h. After cooling to room temperature, the bulk g-C_3N_4 was ground into a fine powder in a mortar and which was labelled as CN.

2.2.2. Synthesis of In_2O_3/g-C_3N_4 photocatalysts

The In_2O_3/g-C_3N_4 heterojunction photocatalysts were prepared by ball milling and heating methods. Typically, 1 g of CN powder and 0.21 g of indium acetate were added to the ball mill jar and ball milled at 250 rpm for 1.5 h. The ratio of zirconium dioxide balls to powder was 100:1. Then, the uniformly mixed g-C_3N_4 and indium acetate powders were transferred to an alumina crucible and heated in air at 5 °C/min to 550 °C for 4 h. After cooling, a In_2O_3/g-C_3N_4 heterojunction catalyst was obtained and was flagged as In_2O_3/CN. By adjusting the amount of indium acetate, different ratios of In_2O_3/g-C_3N_4 photocatalysts were prepared in the same way. Herein, the catalysts which synthesized with 0.021, 0.105, 0.210, 0.315 and 0.420 g of indium acetate and 1 g of CN were marked as 1%In_2O_3/CN, 5%In_2O_3/CN, 10%In_2O_3/CN, 20%In_2O_3/CN and 30%In_2O_3/CN, respectively. Pure In_2O_3 was gotten directly by heating indium acetate without addition of CN.

2.3. Characterization

The microscopic morphology and polycrystalline features of samples were investigated by scanning electron microscopy (SEM, Regulus 8100, Hitachi, Japan) and transmission electron microscopy (TEM, FEI F200, JEOL, Japan). Automatic specific surface and porosity analyzer (Micromeritics ASAP2020, USA) was used to analyze the specific surface area and pore size distribution. The X-ray diffraction (XRD, D8 ADVANVE, Bruker, Germany) and X-ray photoelectron spectra (XPS, Thermo scientific K-Alpha, USA) were employed to study the crystalline structure and chemical state of samples, respectively. The in-situ irradiation XPS (PHI5000, ULVAC-PHI. INC.) was employed to demonstrate the type of In_2O_3/CN heterojunction. The Fourier transforms infrared spectroscopy (FT-IR, Thermo NICOLET IS10, USA) was used to detect the functional groups of samples at wavenumbers ranging from 400 cm^{-1} to 4000 cm^{-1}. The UV–vis diffuse reflectance spectra (DRS) were measured with a UV–vis spectrophotometer (Shimadzu UV-3600, Japan). In addition, the Steady-state photoluminescence (PL) spectra were obtained by a fluorescence spectrometer (Hitachi, F-700) at an excitation wavelength of 345 nm, and Time-resolved transient photoluminescence (TRPL) spectra was measured by Edinburgh FLS1000 spectrometer.

2.4. Electrochemical measurements

An electrochemical workstation (CHI-760E, China) was employed to analyze the optical and electrochemical properties of the samples, including transient photocurrent response, electrochemical impedance spectra (EIS), and Mott Schottky curves. In a 0.2 M Na_2SO_4 electrolyte solution, Ag/AgCl and Pt (1 ×1 cm^2) were employed as the reference electrode and counter electrode, respectively. In the preparation of working electrode, 25 mg of the sample was dispersed in a mixture ink (400 μL deionized water, 100 μL isopropanol, 20 μL Nafion) and sonicated for 15 min. A 25 μL of the suspension was dropped onto 1 × 1 cm^2 fluorine tin oxide (FTO) conductive glass. The 420 W xenon lamp provides light to obtain EIS at frequencies from 1 to 100,000 Hz. The flat-band potentials of the samples were determined by the Mott Schottky method at 1000 Hz.

2.5. Culture and enumeration of colony

Escherichia coli (*E. coli*, ATCC25922) and *Bacillus subtilis* (*B. subtilis*, ATCC6633), as representatives of Gram-negative and Gram-positive bacteria, respectively, were selected as target pollutants in this study [26]. The cell suspension was prepared in the following steps. Firstly, the bacterial cells were cultured in nutrient broth growth medium at 37 °C for approximately 16 h to reach the logarithmic phase. The cultured bacteria were then centrifuged and washed with sterilized deionized water (instruments and solutions related to bacteria were autoclaved at 121 °C for 20 min), and the resuspension-centrifugation

was repeated three times. Simulated wastewater with an initial cell concentration of 1×10^6 CFU/mL was prepared by adjusting the amount of cell suspension. Each photo catalytically disinfected sample was diluted with an appropriate gradient of 0.9% NaCl sterile solution. A 0.3 mL of the diluted sample was evenly spread on LB agar plates and incubated at 37 °C for 24 h. Each experiment was repeated three times and the number of colonies was recorded to quantify viable or culturable bacterial cells. The detection limit of *E. coli* and *B. subtilis* colonies was 4 CFU/mL.

2.6. Photocatalytic experiments

The photocatalytic sterilization activity of the In_2O_3/CN was evaluated under simulated solar radiation. Experiments were conducted with an irradiation intensity of 800 W/m^2 provided by a solar simulator (SOLARBEAM-04–3A, CROWNTECH, INC. USA). Add 120 mg photocatalyst to 200 mL bacterial suspension (1×10^6 CFU/mL) and stir in the dark for 20 min. After the blank sample was taken, the mixed solution was transferred to simulated sunlight to start disinfection. During the experiment, a low temperature constant temperature stirring reaction bath was used to maintain the temperature of 25 °C and stirring rate of 200 rpm. 1 mL of the mixed solution was extracted every 30 min, and the bacteria were cultured and counted. The initial pH of the reaction system was 5.5, which was adjusted with NaOH and Na_2SO_4 when investigating the effect of pH on photocatalytic disinfection. Each experiment was repeated three times.

To investigate the applicability of In_2O_3/CN heterojunctions, actual wastewater disinfection and actual photocatalytic tests were performed, respectively. For this purpose, municipal sewage, lake water and aquaculture wastewater were collected for photocatalytic deactivation experiments from Fuzhou and Zhangzhou cities in Fujian Province, China, respectively. The water matrix parameters of the wastewater can be found in Table S1 of the Supplementary Information. In addition to this, *E. coli* was introduced to ensure a bacterial concentration of 1×10^6 CFU/mL. The inactivation experiment under natural light irradiation was carried out outdoors in Fujian Normal University in October and November 2022, and the temperature and natural light intensity during disinfection were monitored.

RS generated during the photocatalytic process were confirmed by quenching experiments and ESR detection, the specific experimental conditions can be found in Text S1.

2.7. Evaluation of cell activity

Details information for identifying cell viability (including SEM morphological analysis, DNA agarose gel electrophoresis, cell regrowth test) can be found in Text S2.

3. Results and discussion

3.1. Composition and morphology of the photocatalysts

To determine the chemical composition of the In_2O_3/CN, pure CN, In_2O_3, and a series of In_2O_3-modified CN were characterized by X-ray powder diffractometry (XRD). As shown in Fig. 1, pure In_2O_3 has four distinct diffraction peaks at 30.6°, 35.6°, 50.9° and 60.8°, which are attributed to the (2 2 2), (4 0 0), (4 4 0) and (6 2 2) crystal planes of the cubic In_2O_3 (JCPDS No. 71–2194), respectively. The pure CN has two main diffraction peaks at around 13.1° and 27.4°, corresponding to the repetitive pattern of the in-plane structure of the aromatic system and the interlayer reflection of the graphite structure, respectively. Evidently, the diffraction peaks of In_2O_3 and CN were exhibited in all In_2O_3/CN photocatalysts. With the gradual increase of In_2O_3 addition, the diffraction peaks of In_2O_3 exhibit a corresponding enhancement. While, the diffraction peaks of CN decrease, indicating the presence of crystalline phases of In_2O_3 and CN in the samples. Therefore, XRD
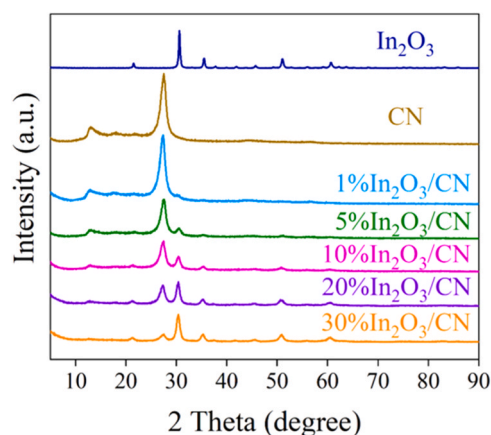

Fig. 1. XRD pattern of pure CN, In_2O_3 and In_2O_3/CN (1, 5, 10, 20, 30% In_2O_3/CN).

analysis revealed that the overall crystal form of CN was not destroyed after modifying In_2O_3, and In_2O_3 was successfully combined with CN.

To further confirm the successful synthesis of In_2O_3/CN heterojunctions, the microscopic morphology and bonding structure were characterized by TEM and HRTEM, as shown in Fig. 2a and b. It is evident that pure CN presents an irregular sheet shape, which can be attributed to the susceptibility of its lattice structure to electron beam irradiation-induced collapse. It is consistent with previous studies [27, 28]. In addition, the TEM image (Fig. 2c) of In_2O_3/CN shows numerous In_2O_3 dispersed on the CN layer. The HRTEM image (Fig. 2d) shows a lattice spacing of 0.293 nm from the (2 2 2) crystal plane, which is a morphological characteristic ascribed to In_2O_3. Overall, morphological features attributed to CN and lattice fringes attributed to In_2O_3 are observed on the surface of In_2O_3/CN, confirming the successful construction of a heterojunction interface.

Fig. S1 shows the scanning electron microscope (SEM) images of CN and In_2O_3/CN. Compared to pure CN, the surface morphology of In_2O_3/CN is rougher and dispersed with numerous fine particles, which are most likely indium oxide particles. To confirm this, Energy Dispersive Spectroscopy (EDS) analysis of In_2O_3/CN was performed. As shown in Fig. 2e-i, the distribution of In and O exhibit significant overlapped, and those of C and N are consistent, indicating that In_2O_3 is successfully loaded onto CN. Reinforcing the findings of TEM, SEM and EDS analysis, further confirmed the successful preparation of the In_2O_3/CN heterojunction.

The porous properties of CN and In_2O_3 may change after doping process, which were characterized by BET and Barrett-Joyner-Halenda (BJH) methods (Fig. S2). The data presented in Table 1 suggest that samples are primarily exhibit mesoporous structures, with the latter possessing smaller pore sizes. The specific surface area of CN and In_2O_3 were only 5.6 and 4.7 cm^2/g. while, after composing, the specific surface areas was significantly increase to 19.8 cm^2/g, which is favorable to photocatalytic activity. In addition, the pore volumes of pure CN, In_2O_3 and 10% In_2O_3/CN were 0.044, 0.035 and 0.118 cm^3/g, respectively, indicating that In_2O_3 did not block the pore structure of CN. Therefore, the In_2O_3/CN might have better photocatalytic activity.

3.2. XPS and FT-IR analysis of photocatalysts

To reveal the chemical states of CN and In_2O_3/CN catalysts, XPS and FT-IR were conducted. As shown in Fig. 3a, the two peaks at 284.6 and 287.9 eV for 10% In_2O_3/CN are attributed to the sp^2 C–C bond and the sp^2–carbon bond in N-containing aromatic rings (N–C=N) [29], respectively. In addition, the weak shoulder can be deconvoluted to form a peak at 286.2 eV, which can be attributed to the carbon bond in the sp^3-coordination. In consistent with the XPS spectra of pure CN
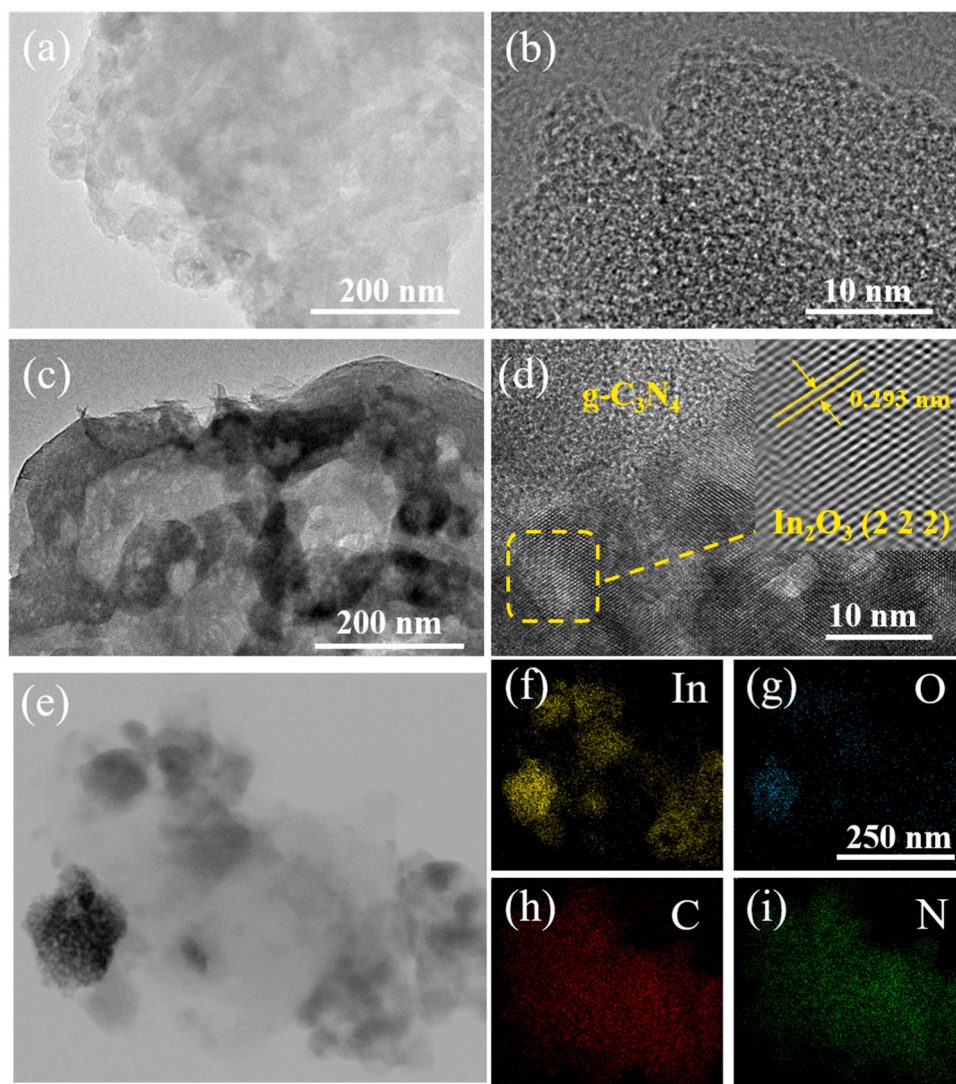
Fig. 2. (a) TEM and (b) HRTEM images of CN; (c) TEM and (d) HRTEM images of 10%In$_2$O$_3$/CN; (e) EDS element mapping of (f) In, (g) O, (h) C, and (i) N.

Table 1
The specific surface areas, pore sizes and pore volume data of catalysts calculated by BET and BJH method.

Sample	Specific surface areas (cm^2/g)	Pore size (nm)	Pore volume (cm^3/g)
g-C$_3$N$_4$	5.6	31.2	0.044
In$_2$O$_3$	4.7	29.3	0.035
10%In$_2$O$_3$/CN	19.8	23.9	0.118

(Fig. S3), g-C$_3$N$_4$ is the major carbon species. In Fig. 3b, the XPS spectra of N 1 s exhibits two clear peaks at binding energies of 398.4 and 401.4 eV, corresponding to the sp^2-bonded N involved in triazine rings (C–N = C) and amino group (C–N–H), respectively. Furthermore, a shoulder peak at a binding energy of 400.3 eV is present, which is ascribed to the action of the tertiary nitrogen N–(C)$_3$ group [30]. The two strong peaks observed in the In 3d spectrum are located at 444.5 and 452.1 eV, respectively, which are classified as In^{3+} in In$_2$O$_3$ crystals (Fig. 3c). Moreover, the peaks at 529.9 and 532.0 eV in the O 1 s can be allocated to oxygen in In$_2$O$_3$ crystal (Fig. 3d). Consistent with the findings of XRD and TEM, XPS analysis provides further evidence that indium oxide was successfully loaded onto the carbon nitride.

As shown in Fig. S4, the FT-IR spectra of pure CN and In$_2$O$_3$/CN with wavelength from 400 to 4000 cm^{-1} were analyzed. All infrared characteristic absorptions related to carbon nitride can be found in the FT-IR spectrum. Among them, the peak near 807 cm^{-1} belongs to the triazine unit, and the characteristic absorption in the range of 1200–1600 cm^{-1} corresponds to the typical tensile vibration of the CN heterocyclic ring [29]. In addition, the peak located in the 3100–3500 cm^{-1} band correspond to the stretching vibration of the O–H of the water molecule and the –NH$_2$ group attached to the sp^2 hybrid carbon [31]. The FT-IR spectrum of In$_2$O$_3$/CN is highly consistent with pure CN due to the lower addition of In$_2$O$_3$ and the more intense IR response of CN.

3.3. Photocatalytic disinfection performances

The photocatalytic activity of the prepared catalysts was evaluated. As shown in Fig. 4a, the concentration of *E. coli* was only decreased by 1.9-log in 180 min without the addition of photocatalyst, indicating that the disinfection performance of simulated sunlight (SSL) alone was not efficiency. Even pure CN and In$_2$O$_3$ was added to the wastewater, only 2.3 and 2.0-log removal was achieved. Thus, the contribution of CN or In$_2$O$_3$ to disinfection is negligible. While, detection limit (approximately 5.8-log removal) was achieved within 90 min by In$_2$O$_3$/CN, indicating that the combination of In$_2$O$_3$ and CN significantly enhanced the photocatalytic disinfection efficiency. To further determine the photocatalytic activity of In$_2$O$_3$/CN, the disinfection performance of In$_2$O$_3$/CN
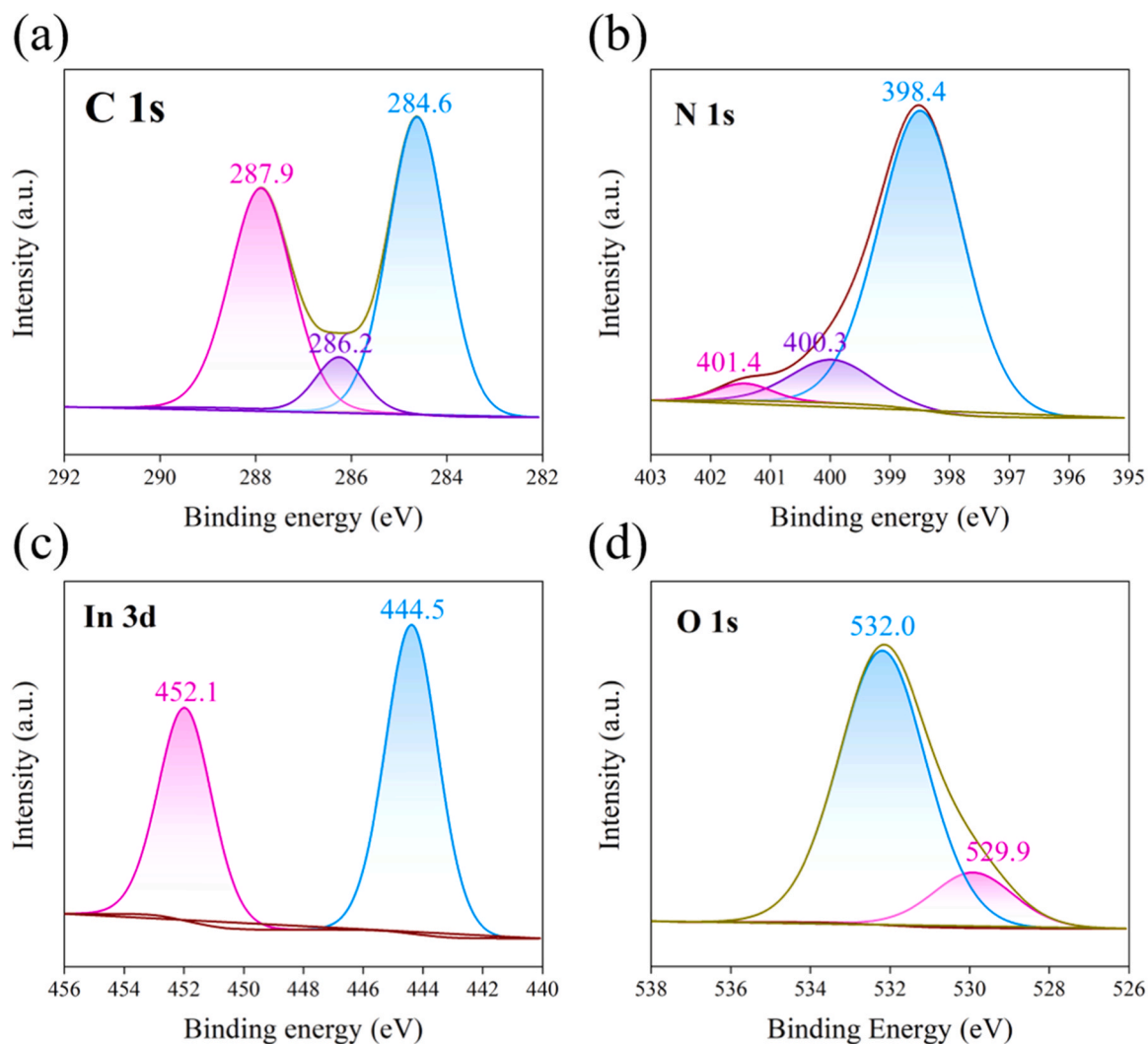
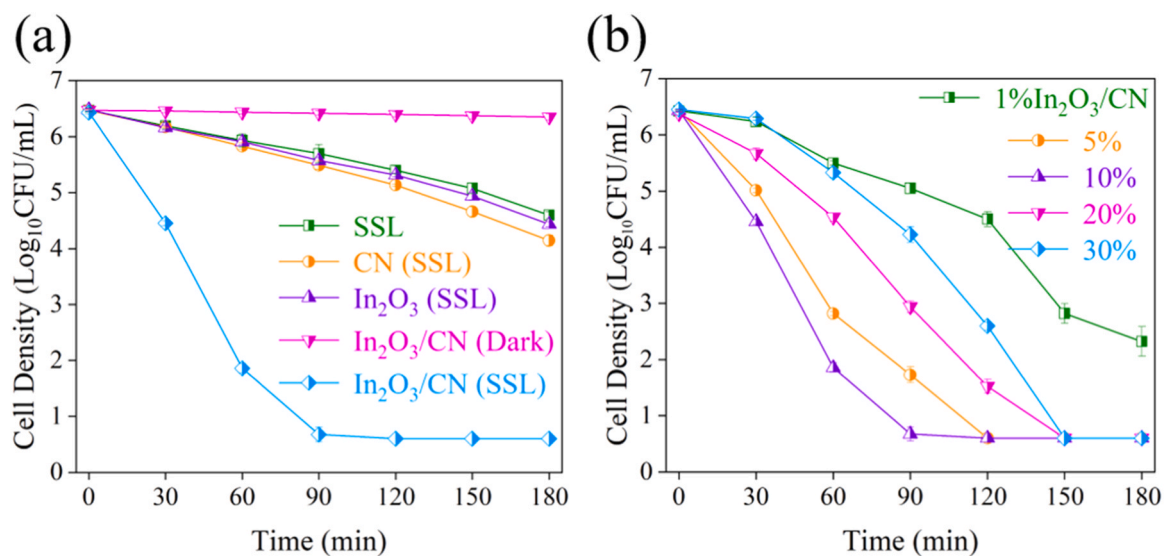**Fig. 3.** (a) The C 1 s, (b) N 1 s, (c) In 3d and (d) O 1 s XPS spectra of 10%In$_2$O$_3$/CN.

Fig. 4. Disinfection performance of (a) different systems and (b) In$_2$O$_3$ to CN ratios.

(1, 5, 10, 20, 30%In$_2$O$_3$/CN) with different In$_2$O$_3$ contents was investigated. It can be clearly observed from Fig. 4b that as the percentage of In$_2$O$_3$ increased, the disinfection performance was enhanced initially and then inhibited. Among them, 10% In$_2$O$_3$/CN had the optimum disinfection efficiency, inactivating about 10^6 CFU/mL *E. coli* only required 90 min's treatment. Overall, the photocatalytic activity of CN can be significantly enhanced by modifying with In$_2$O$_3$, which might be associated with light absorption and reactive species generation. In addition, the concentration of In$_2$O$_3$/CN also affects the disinfection performance. As shown in Fig. S5, the disinfection efficiency gradually increased as the concentration of the catalyst increased from 50 to 400 mg/L, which was attributed to the involvement of more active sites in the photocatalytic reaction. However, further increasing the concentration of In$_2$O$_3$/CN was detrimental to disinfection. It was because excessive catalyst reduced the transmission of sunlight, thereby inhibiting the photocatalytic reaction. Based on the above studies, it can be determined that the photocatalytic disinfection performance of CN was significantly through modifying with In$_2$O$_3$. It may be attributed to the formation of heterojunction structure between In$_2$O$_3$ and CN, which facilitated reactive species (RSs) generation. The In$_2$O$_3$/CN exhibited superior disinfection performance compared to some recent reports on CN-based photocatalysts (Table S2). Therefore, it is necessary to elucidate the disinfection mechanism of In$_2$O$_3$/CN photocatalysts for their enhanced practical applications.

3.4. RSs identification and heterojunction determination

Normally, the disinfection performance of photocatalysts relies on the reactive species generated during photocatalytic reaction, as RSs with strong oxidation tend to kill bacteria indiscriminately [32]. To reveal the contribution of different reactive species (including HO$^\bullet$, O2$\bullet$ − , ^{1}O$_2$ and h$^+$) to *E. coli* inactivation during the disinfection process, quenching experiments and ESR detection were performed. As shown in Fig. 5a, disinfection efficiencies showed a slight decrease respectively, when HO$^\bullet$ and ^{1}O$_2$ were quenched by IPA and L-His. Thus, HO$^\bullet$ and ^{1}O$_2$ were not the dominate RS for *E. coli* inactivation, especially ^{1}O$_2$. The ESR spectra of HO$^\bullet$ and ^{1}O$_2$ were detected with DMPO and TEMP. Fig. 5b showed the typical characteristic peaks with intensity of 1:2:2:1 of DMPO-HO$^\bullet$. Additionally, the characteristic peaks of ^{1}O$_2$ did not be detected by ESR spectra (Fig. S6), which further confirmed that the concentration of ^{1}O$_2$ on disinfection was negligible. In comparison to the absence of scavengers, the presence of SO and TEMPOL significantly suppressed disinfection efficiency by 17% and 36%, respectively. This indicates that h$^+$ and O2$\bullet$ − played essential roles in the photocatalytic process. As shown in Fig. 5c and d, DMPO and TEMPO were employed to capture O2$\bullet$ − and h$^+$, respectively [33]. The typical DMPO-O2$\bullet$ − peaks were observed and the intensity increased over time, indicating continuous generation of O2$\bullet$ − during the catalytic process with In$_2$O$_3$/CN. Furthermore, the peak of TEMPO-h$^+$ significantly decreased over time increased, demonstrating that numerous h$^+$

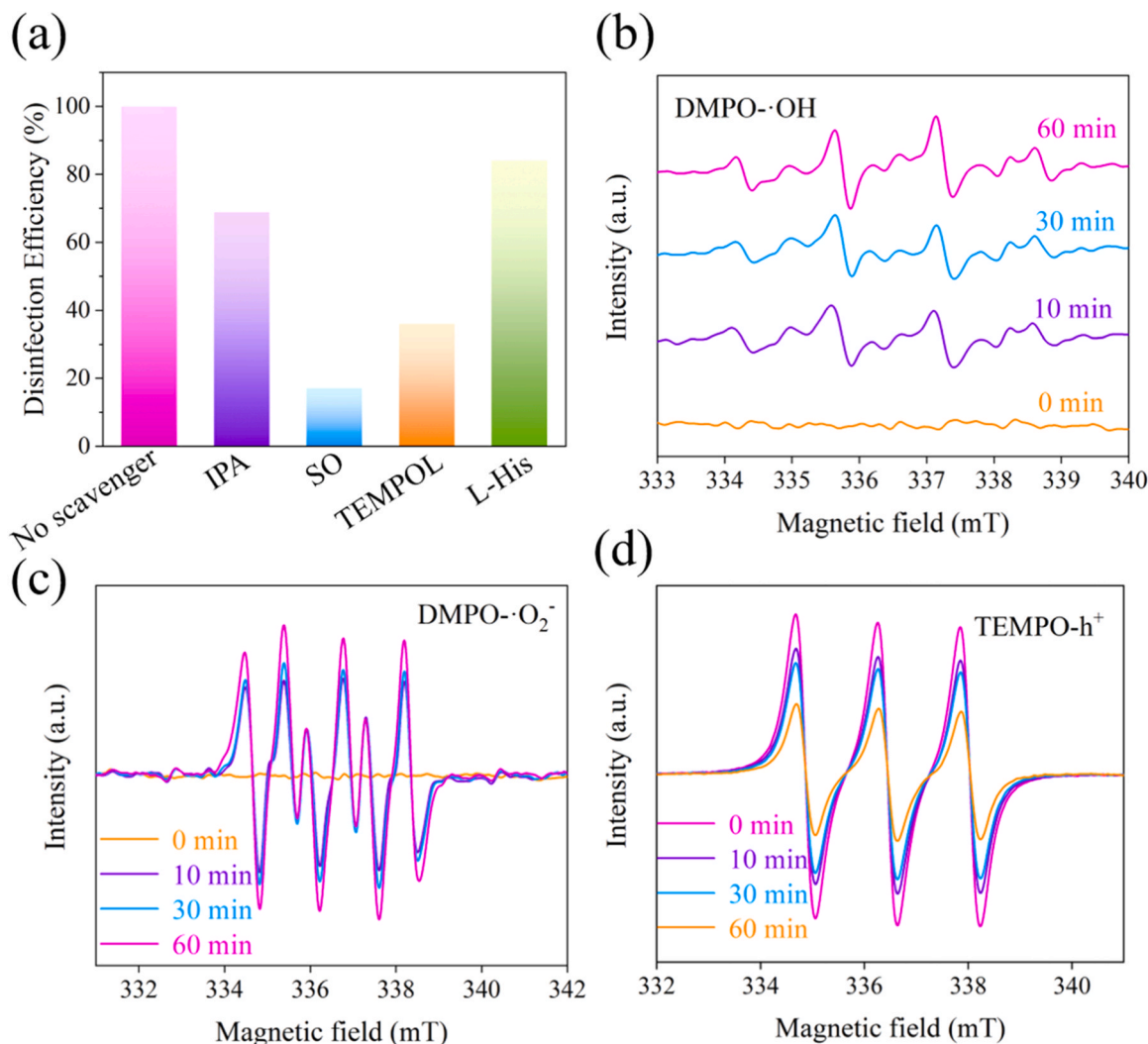**Fig. 5.** (a) Effect of different RS's scavengers on the Disinfection efficiency; ESR spectra of (b) DMPO-HO$^\bullet$, (c) DMPO-O2$\bullet$ − and (d) TEMPO-h$^+$.

was produced during the inactivation of *E. coli*. In summary, it can be inferred that h^+ and $O2\bullet-$ are the primary reactive species in the photocatalytic disinfection process with In_2O_3/CN. In addition, $HO^\bullet$ also played a role in the disinfection process. Therefore, revealing the radical generation pathways of In_2O_3/CN under sunlight is essential to comprehending the disinfection mechanism.

The formation of RSs during photocatalytic disinfection is closely related to the charge separation and energy level structure of the photocatalyst [34]. First of all, transient photocurrent response and electrochemical impedance spectroscopy (EIS) were employed to evaluate the charge separation efficiency of the samples. It can be clearly observed that both CN and In_2O_3/CN produce a photocurrent response under visible light, which means that the samples have formed electron-hole (e^-/h^+) pairs through the photoreaction (Fig. 6a). Apparently, the photocurrent response of In_2O_3 was significantly stronger than that of pure CN, indicating that In_2O_3/CN effectively enhanced the separation of photogenerated carriers. To further verify the charge transfer rate, the samples were characterized by EIS method (Fig. 6b). As expected, the arc radius of In_2O_3/CN is significantly smaller than that of pure CN. It is known that a smaller arc radius in the Nyquist diagram implies a lower charge transfer resistance, which is benefit for charge separation [35]. Thus, the charge transfer efficiency of CN was significantly improved after modifying with In_2O_3.

The charge separation efficiency of In_2O_3/CN was further investigated by steady-state PL emission spectra and time-resolved PL (TRPL) decay spectra. Under the excitation wavelength of 350 nm, pure CN exhibits a strong emission signal around 470 nm, which is attributed to the electronic transition of the π–π * orbital within the triazine structure of CN [36]. However, after modifying with In_2O_3, the intensity of the emitted signal is significantly weaker, indicating that electronic recombination is being suppressed. In contrast, In_2O_3/CN (1.45 ns) exhibits a shorter average radiative lifetime (Table 2) than pure CN (2.49 ns), suggesting a rapid transfer of excited electrons between CN and In_2O_3 crystals [12]. Overall, the aforementioned findings strongly confirm that combining In_2O_3 with CN accelerates charge transfer, facilitates charge separation and reduces charge recombination.

Excellent optical and photoelectrochemical properties allow In_2O_3/CN to have good disinfection properties. helps to understand the

Table 2
Average emission lifetimes of CN and In_2O_3/CN.

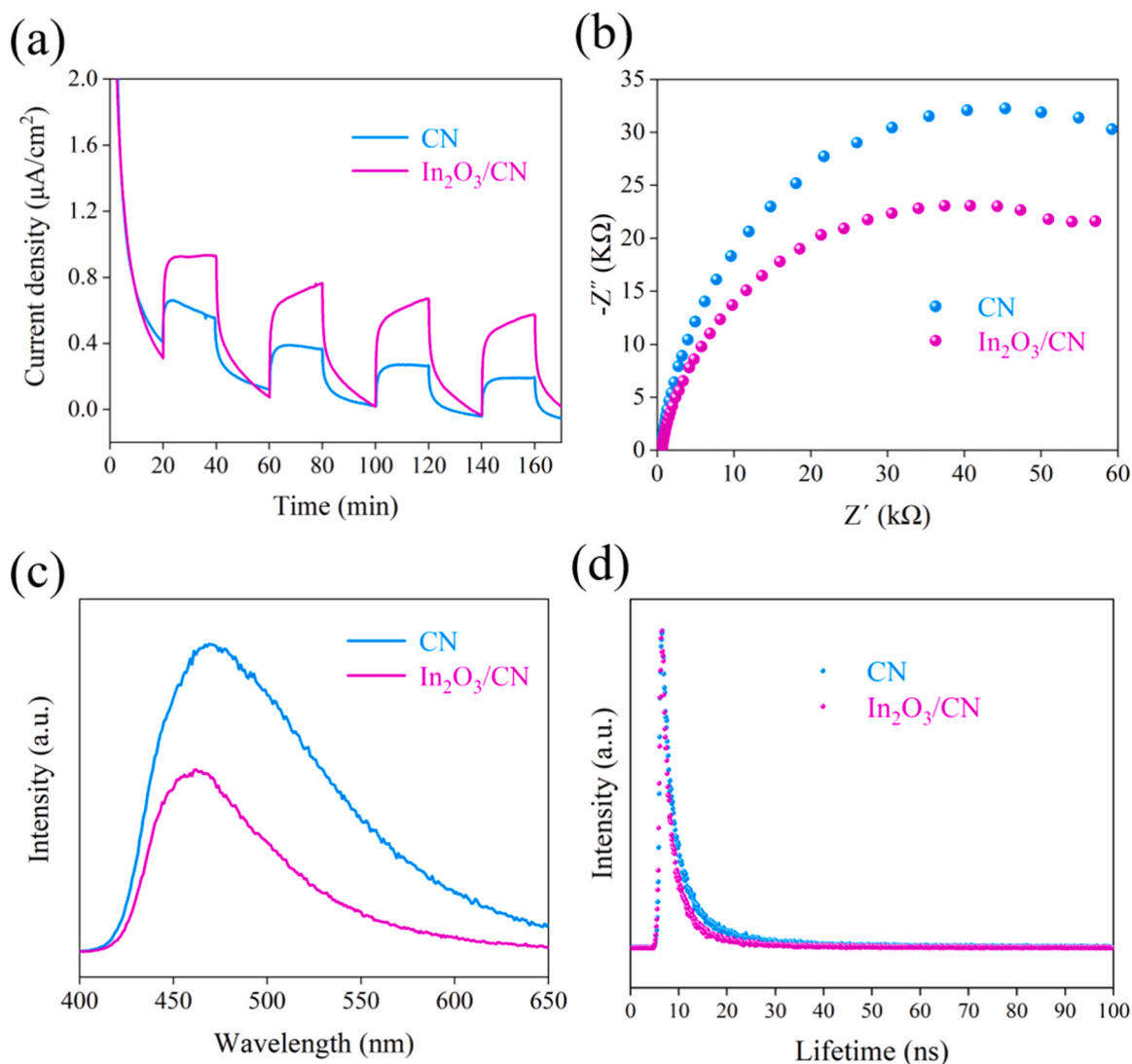| Sample	τ_1 (ns)	B_1 (%)	τ_1 (ns)	B_2 (%)	τ_1 (ns)	B_3 (%)	τ_A (ns)
CN	1.88	31.60	6.39	49.81	35.03	18.59	2.49
10%In_2O_3/ CN	1.39	35.81	4.57	49.01	22.59	15.17	1.45

Fig. 6. The (a) transient photocurrent response, (b) EIS Nyquist plots, (c) PL spectra and (d) time-resolved PL decay spectra of CN amd 10%In_2O_3/CN.

production pathways of RSs and reveal the disinfection mechanisms, the energy band structure of the photocatalyst was analyzed. The UV–vis diffuse reflectance spectroscopy (DRS) was utilized to investigate the light absorption properties of the CN, In_2O_3 and a series of In_2O_3/ CN. As shown in Fig. 7a, the absorption edge of In_2O_3 locates at around 350–430 nm, while CN presents a light absorption between 410 and 440 nm. Compared with pure In_2O_3, the optical absorption properties of a series of In_2O_3/CN were improved in varying degrees. Among them, the 10%In_2O_3/CN exhibits a significant red shift towards the visible region, which means that it has a better light capture capability. In order to determine the band gap of the samples, the transformed Kubelka-Munk function was calculated according to the following equation: $E_g = 1240/\lambda g$ (eV) [37]. It can be observed from Fig. 7b that the band gaps (E_g) of CN, In_2O_3 and 10%In_2O_3/CN are 2.67 eV, 2.79 eV and 2.53 eV, respectively. Obviously, 10%In_2O_3/CN has the smallest forbidden band width, suggesting that lower energy is required for the electronic transition. To further understand the energy band structure of CN and In_2O_3, the flat band potentials (E_{fb}) are measured by Mott-Schottky method. Fig. S7 illustrated that the slopes of the Mott-Schottky curves for both catalysts are positively correlated, indicating that both CN and In_2O_3 are n-type semiconductors [38]. Based on the intercepts, the E_{fb} values of CN and In_2O_3 are − 1.37 and − 0.12 V (Ag/AgCl, pH = 7), respectively. The normal hydrogen electrode potential is $E_{NHE} = E_{Ag/AgCl} + 0.197$

[27], the E_{fb} of CN and In_2O_3 can be calculated to be − 1.17 and 0.08 eV (NHE, pH =7), respectively. For n-type semiconductors, the conduction band approximates the flat-band potential [36], which leads to the inference that the CB potentials of CN and In_2O_3 are − 1.17 and 0.08 eV, respectively. Furthermore, the VB potentials of CN and In_2O_3 were calculated according to the equation: $E_{CB} = E_{VB} - E_g$, + 1.50 and + 2.72 eV respectively.

It has been established that h^+, $O2 \bullet -$ and $HO^\bullet$ were the main RSs generated in the catalytic process. Therefore, the heterojunction type of In_2O_3/CN (two possible types of Type II and Z-scheme) can be determined by analyzing the formation pathways of reactive species. As shown in Fig. 7c, the conventional Type II mechanism was assumed to govern the transport of photogenerated electrons and holes in In_2O_3/CN heterojunctions. According to the conventional Type II mechanism [39], photogenerated electrons are transferred from the CB of CN to the upper CB of In_2O_3, yet the potential is insufficient to induce the production of $O2 \bullet -$ ($O_2/O2 \bullet - = -0.33$ eV vs NHE) [40]. Similarly, the photodissociation hole migrates from the VB of In_2O_3 to the VB of CN, but the potential here is unable to induce H_2O to generate $HO^\bullet$ via the oxidation pathway ($HO^\bullet/OH^- = +1.99$ eV vs NHE) [41]. Obviously, the Type II mechanism is inconsistent with the detection results of reactive species. While, the CB of CN (-1.17 eV vs NHE) is more negative than the standard potential of $O_2/O2 \bullet -$ (-0.33 eV vs NHE) (Fig. 7d). This
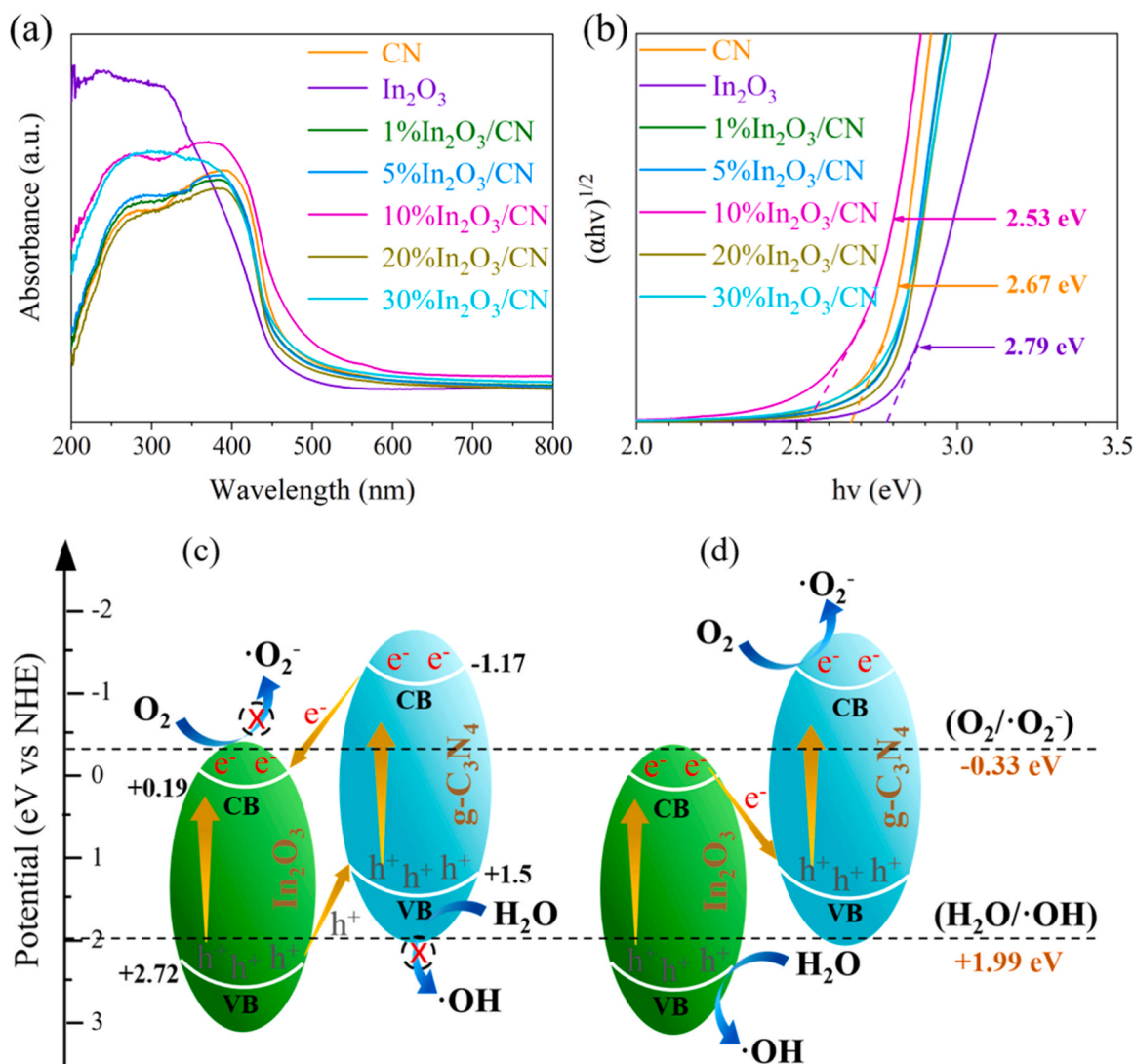

Fig. 7. The (a) DRS spectra and the (b) transformed Kubelka-Munk function of samples; Two possible heterojunctions of (c) Type II and (d) Z-scheme in In_2O_3/CN photocatalyst.

characteristic endows CN with the capacity to induce $O_2^{\bullet-}$

production. Furthermore, although the VB position of CN (+1.50 eV vs NHE) is insufficient for $HO^{\bullet}$ production. The $HO^{\bullet}$ formation in In_2O_3 crystals is thermodynamically favored because of its more positive VB position (+ 2.72 eV vs NHE) than the standard potential of $HO^{\bullet}/OH^-$ (+1.99 eV vs NHE). Consequently, the charge migration of In_2O_3/CN heterojunctions is most probably following the Z-scheme mode. Importantly, the Z-scheme type charge transfer pathway on the In_2O_3/CN heterojunction not only promotes charge separation but also preserves the redox sites for RSs generation. This accounts for the significant enhancement of CN's photocatalytic disinfection performance after modifying with In_2O_3.

To further demonstrate the mode of the In_2O_3/CN heterojunctions, the samples were characterized using in situ irradiated XPS. As shown in Fig. S8, under irradiation, the binding energy of N1s decreased by 0.37 eV, while that of In 3d increased by 0.48 eV. In general, a loss of electrons leads to an increase in binding energy. Thus, these results indicate that electrons are transferred from In_2O_3 to g-C_3N_4 in In_2O_3/CN heterojunction and suggest that this structure follows a Z-scheme structure.

3.5. Bacterial inactivation mechanisms

It can be observed from Fig. 8a, untreated *E. coli* exhibits a typical rod-like structure with complete and smooth cell membrane. Although cells exposed to sunlight alone for 120 min exhibit slight wrinkles (Fig. S9), They still remained active. However, when *E. coli* cell was treated under sunlight with In_2O_3/CN for 120 min, the cell membrane exhibited notable wrinkles and ruptures (Fig. 8b). The cell membrane is widely recognized as a crucial protective barrier that selectively regulates the entry of extracellular substances and maintains diverse

metabolic activities within the cell [42]. It had been confirmed that the RSs (h^+, $O_2^{\bullet-}$ and $HO^{\bullet}$) can attack cell membranes, including peptidoglycans, lipopolysaccharides and phospholipid bilayers [43,44]. While, membrane rupture did not mean complete inactivation. Bacteria could realize reactivation by self-repair [6,45]. Thus, the genomic DNA was analyzed (Fig. 8c). Compared with the samples treat under other conditions, the genomic DNA of the sample treated under sunlight with In_2O_3/CN disappeared, demonstrating that the DNA was completely degraded. Actually, reactive species generated by photocatalytic reaction can cleave the phosphodiester bonds in base pairs, and thus breaking single or double strands of DNA [43]. Damage to the genetic component of *E. coli* leads to complete inactivation. To verify this hypothesis, the treated water was stored in the dark for 24 and 48 h. As shown in Fig. 8d, no re-growth colony was found in the treated water, which indicated complete inactivation of *E. coli*.

3.6. The applicability of In_2O_3/CN for water disinfection

To assess the practical feasibility of In_2O_3/CN photocatalytic disinfection process, its disinfection performance in natural sunlight, actual wastewater, cycling experiments and various influencing factors was studied. First, the photocatalytic disinfection performance of In_2O_3/CN under natural sunlight was investigated, as shown in Fig. S10. It can be clearly observed from Fig. 9b that the treatment time required to achieve complete disinfection under natural sunlight is shorter than that under simulated sunlight. As can be seen from Fig. 9a, water temperature increased to about 35 °C under the sunlight. It had been confirmed that when the temperature closes to the optimum culture temperature (37 °C), the cells are metabolically active and more vulnerable to attack by RSs [26]. It was also verified by the following experiments which investigated the influence of temperature on disinfection (Fig. S11). The
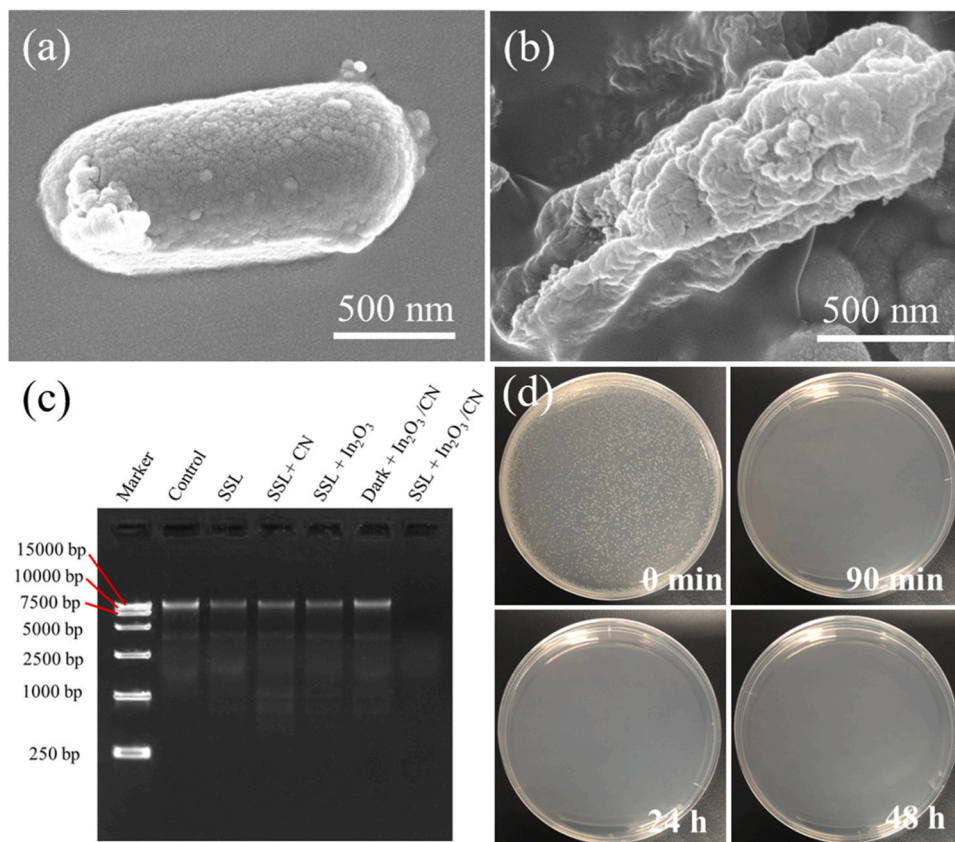

Fig. 8. SEM images of (a) untreated *E. coli* and (b) treated with In_2O_3/CN; (c) DNA fluorescent bands of *E. coli* treated with different systems and (d) *E. coli* regrowth test.
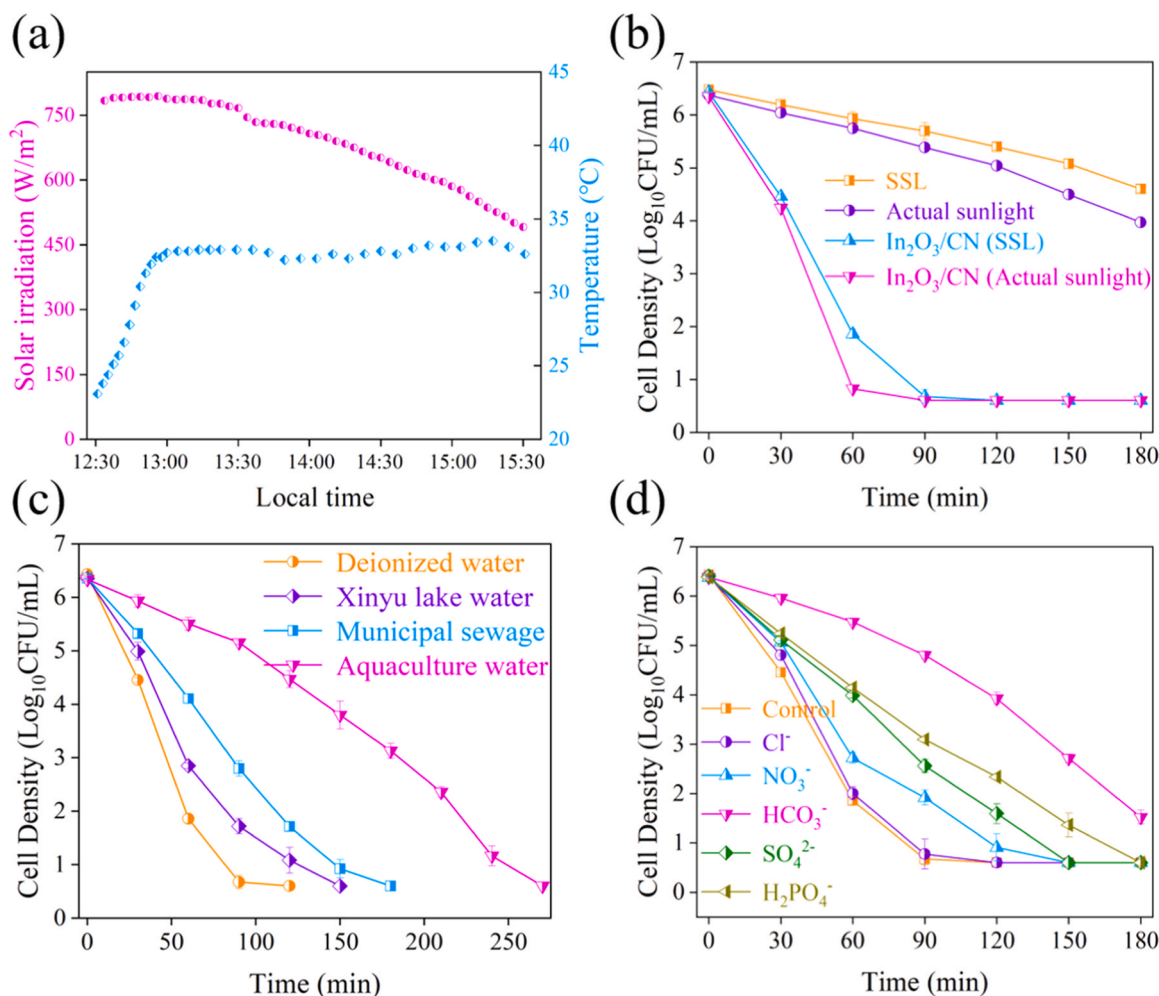
Fig. 9. (a) Irradiation and solution temperature changes, (b) the photocatalytic disinfection performance of In_2O_3/CN under natural sunlight; Effect of (c) actual wastewater (10%In_2O_3/CN with 400 mg/L) and (d) anions (with concentration of 1 mg/L) on disinfection performance.

results show that the In_2O_3/CN photocatalyst also had an excellent disinfection performance under natural sunlight. In addition to its bacteriostatic effect against *E. coli*, In_2O_3/CN exhibited activity against *B. subtilis* (Fig. S12), indicating its potential for inactivating both Gram-positive and Gram-negative organisms.

The composition of real water is complex (Table S1), which may interfere with In_2O_3/CN photocatalytic disinfection. Therefore, the disinfection performance of In_2O_3/CN on three real water was explored (Fig. 9c). Compared with that for deionized water, longer treatment time was required for real water and followed the order: Xinyu Lake water < Municipal sewage < Aquaculture water. Despite the complexity of the water matrix in three real water samples, complete disinfection could be achieved by the photocatalytic disinfection process with In_2O_3/CN. To further investigate the effect of water matrix on the photocatalytic disinfection process, the influences of humic acid (HA) and anions was explored. [46]. It can be observed from Fig. S13, HA at a concentration of 1 mg/L significantly enhanced *E. coli* inactivation. While, further increasing the HA concentration would inhibit disinfection. HA is a photosensitive substance that can be excited by light to reach a triplet excited state (^{3}DMO*) [47]. ^{3}DMO* reacts with the cell membrane and destroys membrane, enhancing disinfection process [48]. However, as the concentration of HA increases, sunlight irradiation tends to be absorbed by HA, thus weakening the photocatalytic activity of In_2O_3/CN and inhibiting disinfection [4]. The influences of inorganic anions on the photocatalytic disinfection were also investigated (Fig. 9d). Besides Cl^-, the presence of NO_3^-, SO_4^{2-}, HCO_3^- and $H_2PO_4^-$ inhibited disinfection

efficiency. Because these ions could form a charge layer on the surface of the In_2O_3/CN heterojunction, thereby repelling *E. coli* and impeding cell inactivation [49,50]. Among them, the inhibition of HCO_3^- and $H_2PO_4^-$ was more significant. It is because they can react with $HO^\bullet$ to produce less reactive radical ($\bullet CO_3^-$ and $\bullet HPO_4^-$) [49,51]. Although these unfavorable water matrixes were present, more than 10-log removal can be achieved within 180 min during the photocatalytic process with In_2O_3/CN. Additionally, the influence of solution pH value on the In_2O_3/CN photocatalytic disinfection performance was also investigated (Fig. S14). Apparently, the inactivation efficiency of *E. coli* decreases as the solution pH value increases. As far as we know, an increase in solution pH value greatly reduces the oxidation potential of $HO^\bullet$ and $O2\bullet-$ [52], which is not conducive to bacterial disinfection. Nevertheless, the inactivation efficiency of *E. coli* could be improved by prolonging the photocatalytic reaction time.

Reusability is a key factor in evaluating the practicality of photocatalysts. For this purpose, the stability of the photocatalyst was assessed by studying the reusability of the In_2O_3/CN heterojunction. As shown in Fig. 10a, the disinfection efficiency only showed a slight decrease after 5 cycles. The *E. coli* was still able to be completely inactivated (~5.8-log removal) within 120 min, indicating that the In_2O_3/CN photocatalysts have a good reusability. To further validate this result, samples after 5 cycles were collected and characterized using XRD and FT-IR (Figs. 10b and 10c). Compared to fresh In_2O_3/CN, the specific positions of the XRD characteristic peaks of the samples did not change after use and only showed a slight weakening, indicating that the heterojunction structure
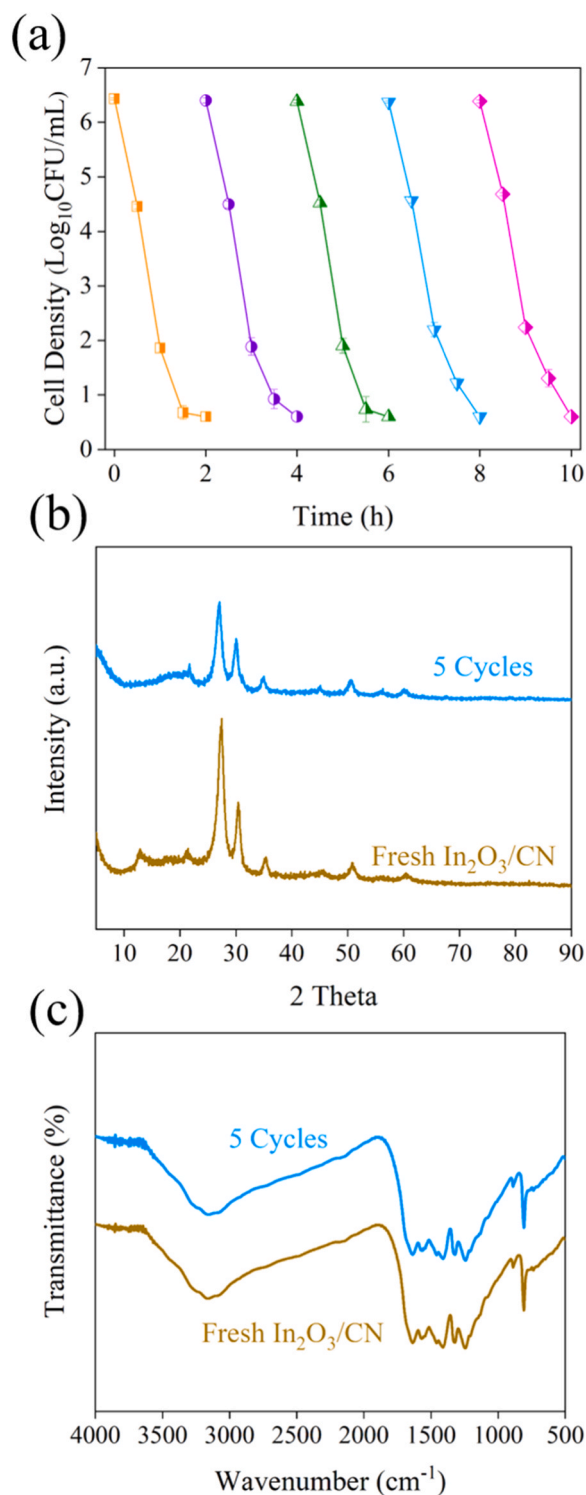
Fig. 10. (a) The cycling tests of In_2O_3/CN; (b) XRD and (c) FT-IR spectra of In_2O_3/CN before and after usage.

(Fig. S15), which further proved that the structure of In_2O_3 remained intact and there was no risk of metal ions leaching.

4. Conclusions

In this study, Z-scheme In_2O_3/CN heterojunctions were successfully prepared and applied to photocatalytic disinfection under sunlight. Detection limit (about 5.8-log removal) could be achieved within 90 min. Benefiting from the formation of a heterojunction structure between In_2O_3 and CN, the photocatalyst exhibits significantly broadened light absorption range and effectively suppressed photogenerated charge recombination. Besides the photogenerated h^+, $O2 \bullet -$ and $HO^\bullet$ generated under sunlight irradiation through redox reaction were the main RSs for bacterial inactivation. Not only cell integrity structure but also genomic DNA were destroyed by the photocatalytic process with In_2O_3/CN, and complete disinfection was achieved. In_2O_3/CN also exhibit a perfect disinfection performance under natural sunlight. Although more treatment time was required, detection limit was still achieved for different actual wastewater treatment or in the presence of HA and different inorganic anions. Therefore, the photocatalytic disinfection process with In_2O_3/CN is a promising option for water disinfection.

CRediT authorship contribution statement

Yanchao Jin and Riyao Chen designed the study. Xiongjian Chen, Yanchao Jin, Peiwen Huang, Zhanwang Zheng, Li-Ping Li, Chun-Yan Lin, Xiao Chen, Rui Ding, Jianxi Liu, Riyao Chen performed the experiments. Yanchao Jin and Riyao Chen analyzed the data and wrote the manuscript. All authors read and approved the final manuscript.

Declaration of Competing Interest

The authors declare that they have no competing interests.

Data availability

Data will be made available on request.

Acknowledgements

Appendix A. Supporting information

Supplementary data associated with this article can be found in the online version at doi:10.1016/j.apcatb.2023.123235.

References

[1] D. Ma, M.H. Weir, N.M. Hull, Fluence-based QMRA model for bacterial photorepair and regrowth in drinking water after decentralized UV disinfection, Water Res 231 (2023), 119612.

[2] X. Chen, Y. Jin, Z. Zhou, P. Huang, X. Chen, R. Ding, R. Chen, Spontaneous nutrient recovery and disinfection of aquaculture wastewater via Mg-coconut shell carbon composites, J. Hazard. Mater. 426 (2021), 128119.

[3] P. Murugesan, J.A. Moses, C. Anandharamakrishnan, Photocatalytic disinfection efficiency of 2D structure graphitic carbon nitride-based nanocomposites: a review, J. Mater. Sci. 54 (2019) 12206–12235.

[4] F. Liu, Z. Li, Q. Dong, C. Nie, S. Wang, B. Zhang, P. Han, M. Tong, Catalyst-Free Periodate Activation by Solar Irradiation for Bacterial Disinfection: Performance and Mechanisms, Environ. Sci. Technol. 56 (2022) 4413–4424.

was not disrupted. The repeated washing and drying resulted in a modification of the crystalline structure of CN (XRD peak at 13.1°), while this did not affect its photocatalytic properties. This was also confirmed by the FT-IR peaks of the samples. Above all, In_2O_3/CN photocatalysts are significantly reusable for disinfection. The indium ion leaching was also during In_2O_3/CN photocatalytic disinfection using inductively coupled plasma emission spectroscopy. The results showed that no indium ion was detected throughout the experimental cycle

[5] D. Guo, S. You, F. Li, Y. Liu, Engineering carbon nanocatalysts towards efficient degradation of emerging organic contaminants via persulfate activation: A review, Chin. Chem. Lett. 33 (2021) 1–10.

[6] Y.-d Chen, X. Duan, X. Zhou, R. Wang, S. Wang, N.-q Ren, S.-H. Ho, Advanced oxidation processes for water disinfection: Features, mechanisms and prospects, Chem. Eng. J. 409 (2021), 128207.

[7] D. Yang, D. Qu, L. An, X. Zong, Z. Sun, A metal-free carbon dots for wastewater treatment by visible light active photo-Fenton-like reaction in the broad pH range, Chin. Chem. Lett. 32 (2021) 2292–2296.

[8] H. Shi, J. Wan, X. Dong, J. Xi, L. Zhang, W. Wang, X. Zhang, Y. Shi, Z. Tang, Ag bridged step-scheme $MoS_2/Bi_4O_5Br_2$ heterojunction for enhanced visible light driven photocatalytic disinfection activity, Appl. Surf. Sci. 607 (2023), 155056.

[9] A. Hu, J. Ye, G. Ren, Y. Qi, Y. Chen, S. Zhou, Metal-Free Semiconductor-Based Bio-Nano Hybrids for Sustainable CO_2-to-CH_4 Conversion with High Quantum Yield, Angew. Chem. Int. Ed. Engl. 61 (2022), e202206508.

[10] J. Ye, C. Wang, C. Gao, T. Fu, C. Yang, G. Ren, J. Lu, S. Zhou, Y. Xiong, Solar-driven methanogenesis with ultrahigh selectivity by turning down H_2 production at biotic-abiotic interface, Nat. Commun. 13 (2022) 6612.

[11] B. Liu, J. Du, G. Ke, B. Jia, Y. Huang, H. He, Y. Zhou, Z. Zou, Boosting O_2 Reduction and H_2O Dehydrogenation Kinetics: Surface N-Hydroxymethylation of g-C_3N_4 Photocatalysts for the Efficient Production of H_2O_2, Adv. Funct. Mater. 32 (2021) 2111125.

[12] Y. Deng, Z. Zhou, H. Zeng, R. Tang, L. Li, J. Wang, C. Feng, D. Gong, L. Tang, Y. Huang, Phosphorus and potassium co-doped g-C_3N_4 with multiple-locus synergies to degrade atrazine: Insights into the depth analysis of the generation and role of singlet oxygen, Appl. Catal. B 320 (2023), 121942.

[13] Y. Shi, J. Ma, Y. Chen, Y. Qian, B. Xu, W. Chu, D. An, Recent progress of silver-containing photocatalysts for water disinfection under visible light irradiation: A review, Sci. Total Environ. 804 (2022) 150024.

[14] S. Cao, J. Low, J. Yu, M. Jaroniec, Polymeric photocatalysts based on graphitic carbon nitride, Adv. Mater. 27 (2015) 2150–2176.

[15] S. Ma, S. Zhan, Y. Jia, Q. Shi, Q. Zhou, Enhanced disinfection application of Ag-modified g-C_3N_4 composite under visible light, Appl. Catal. B 186 (2016) 77–87.

[16] R. Wang, X. Kong, W. Zhang, W. Zhu, L. Huang, J. Wang, X. Zhang, X. Liu, N. Hu, Y. Suo, J. Wang, Mechanism insight into rapid photocatalytic disinfection of Salmonella based on vanadate QDs-interspersed g-C_3N_4 heterostructures, Appl. Catal. B 225 (2018) 228–237.

[17] J. Lin, W. Tian, Z. Guan, H. Zhang, X. Duan, H. Wang, H. Sun, Y. Fang, Y. Huang, S. Wang, Functional Carbon Nitride Materials in Photo-Fenton-Like Catalysis for Environmental Remediation, Adv. Funct. Mater. 32 (2022) 2201743.

[18] Y. Qiu, Z. Xing, M. Guo, Z. Li, N. Wang, W. Zhou, Hollow cubic Cu₂-xS/Fe-POMs/AgVO₃ dual Z-scheme heterojunctions with wide-spectrum response and enhanced photothermal and photocatalytic-fenton performance, Appl. Catal. B 298 (2021), 120628.

[19] H. Yang, A short review on heterojunction photocatalysts: Carrier transfer behavior and photocatalytic mechanisms, Mater. Res. Bull. 142 (2021), 111406.

[20] C. He, X. Li, D. Qiu, Y. Chen, Y. Lu, X. Cui, Nonlinear optical polarization and heterostructure synergistically boosted the built-in electric field of $CeF_3/LiNbO_3$ for a higher photocatalytic nitrogen reduction activity, Appl. Surf. Sci. 556 (2021), 149753.

[21] Y. Lu, L. Shao, S. Deng, Z. Lu, R. Yan, D. Ren, Y. Huang, H. Liu, Synthesis of C-$In_2O_3/BiOI$ composite and its enhanced photocatalytic degradation for methyl blue, Inorg. Chem. Commun. 100 (2019) 56–59.

[22] P. Chang, Y. Wang, Y. Wang, Y. Zhu, Current trends on In_2O_3 based heterojunction photocatalytic systems in photocatalytic application, Chem. Eng. J. 450 (2022), 127804.

[23] N. Wei, H. Cui, X. Wang, X. Xie, M. Wang, L. Zhang, J. Tian, Hierarchical assembly of In(2)O(3) nanoparticles on ZnO hollow nanotubes using carbon fibers as templates: Enhanced photocatalytic and gas-sensing properties, J. Colloid Interface Sci. 498 (2017) 263–270.

[24] Z. Pan, L. Qian, J. Shen, J. Huang, Y. Guo, Z. Zhang, Construction and application of Z-scheme heterojunction In_2O_3/Bi_4O_7 with effective removal of antibiotic under visible light, Chem. Eng. J. 426 (2021), 130385.

[25] J. Shen, L. Qian, J. Huang, Y. Guo, Z. Zhang, Enhanced degradation toward Levofloxacin under visible light with S-scheme heterojunction In_2O_3/Ag_2CO_3: Internal electric field, DFT calculation and degradation mechanism, Sep. Purif. Technol. 275 (2021), 119329.

[26] Y. Jin, Y. Shi, Z. Chen, R. Chen, X. Chen, X. Zheng, Y. Liu, R. Ding, Enhancement of solar water disinfection using H_2O_2 generated in situ by electrochemical reduction, Appl. Catal. B 267 (2020), 118730.

[27] X. Geng, L. Wang, L. Zhang, H. Wang, Y. Peng, Z. Bian, H_2O_2 production and in situ sterilization over a ZnO/g-C_3N_4 heterojunction photocatalyst, Chem. Eng. J. 420 (2021), 129722.

[28] X. Jin, Q. Guan, T. Tian, H. Li, Y. Han, F. Hao, Y. Cui, W. Li, Y. Zhu, Y. Zhang, In_2O_3/boron doped g-C_3N_4 heterojunction catalysts with remarkably enhanced visible-light photocatalytic efficiencies, Appl. Surf. Sci. 504 (2020), 144241.

[29] S.-W. Cao, X.-F. Liu, Y.-P. Yuan, Z.-Y. Zhang, Y.-S. Liao, J. Fang, S.C.J. Loo, T.C. Sum, C. Xue, Solar-to-fuels conversion over In_2O_3/g-C_3N_4 hybrid photocatalysts, Appl. Catal. B 147 (2014) 940–946.

[30] H. Gao, S. Yan, J. Wang, Y.A. Huang, P. Wang, Z. Li, Z. Zou, Towards efficient solar hydrogen production by intercalated carbon nitride photocatalyst, Phys. Chem. Chem. Phys. 15 (2013) 18077–18084.

[31] L.-Y. Chen, W.-D. Zhang, In_2O_3/g-C_3N_4 composite photocatalysts with enhanced visible light driven activity, Appl. Surf. Sci. 301 (2014) 428–435.

[32] J. Xiao, Q. Liu, M. Song, X. Li, Q. Li, J.K. Shang, Directing photocatalytic pathway to exceedingly high antibacterial activity in water by functionalizing holey ultrathin nanosheets of graphitic carbon nitride, Water Res 198 (2021), 117125.

[33] Z. Sun, X. Yang, X.-F. Yu, L. Xia, Y. Peng, Z. Li, Y. Zhang, J. Cheng, K. Zhang, J. Yu, Surface oxygen vacancies of Pd/Bi_2MoO_6-x acts as "Electron Bridge" to promote photocatalytic selective oxidation of alcohol, Appl. Catal. B 285 (2021), 119790.

[34] Z. Lin, S. Ye, Y. Xu, X. Lin, Z. Qin, J. Bao, H. Peng, Construction of a novel efficient Z-scheme BiVO₄/EAQ heterojunction for the photocatalytic inactivation of antibiotic-resistant pathogens: Performance and mechanism, Chem. Eng. J. 453 (2023), 139747.

[35] K. Dou, C. Peng, R. Wang, H. Cao, C. Yao, J. Qiu, J. Liu, N. Tsidaeva, W. Wang, S-scheme tubular g-C_3N_4/BiOI heterojunctions for boosting photodegradation of tetracycline and Cr(VI): Mechanism insight, degradation pathway and DFT calculation, Chem. Eng. J. 455 (2023), 140813.

[36] L. Shao, D. Jiang, P. Xiao, L. Zhu, S. Meng, M. Chen, Enhancement of g-C_3N_4 nanosheets photocatalysis by synergistic interaction of ZnS microsphere and RGO inducing multistep charge transfer, Appl. Catal. B 198 (2016) 200–210.

[37] T. Sano, S. Tsutsui, K. Koike, T. Hirakawa, Y. Teramoto, N. Negishi, K. Takeuchi, Activation of graphitic carbon nitride (g-C_3N_4) by alkaline hydrothermal treatment for photocatalytic NO oxidation in gas phase, J. Mater. Chem. A 1 (2013) 6489–6496.

[38] V. Vinesh, M. Preeyanghaa, T.R.N. Kumar, M. Ashokkumar, C.L. Bianchi, B. Neppolian, Revealing the stability of CuWO₄/g-C_3N_4 nanocomposite for photocatalytic tetracycline degradation from the aqueous environment and DFT analysis, Environ. Res. 207 (2022), 112112.

[39] Y. Liu, X. Zeng, X. Hu, J. Hu, Y. Wang, Y. Yin, C. Sun, X. Zhang, Two-dimensional g-C_3N_4/TiO₂ nanocomposites as vertical Z-scheme heterojunction for improved photocatalytic water disinfection, Catal. Today 335 (2019) 243–251.

[40] H. Sheng, H. Zhang, W. Song, H. Ji, W. Ma, C. Chen, J. Zhao, Activation of Water in Titanium Dioxide Photocatalysis by Formation of Surface Hydrogen Bonds: An In Situ IR Spectroscopy Study, Angew. Chem. Int. Ed. Engl. 54 (2015) 5905–5909.

[41] W. Wang, J.C. Yu, D. Xia, P.K. Wong, Y. Li, Graphene and g-C_3N_4 nanosheets cowrapped elemental alpha-sulfur as a novel metal-free heterojunction photocatalyst for bacterial inactivation under visible-light, Environ. Sci. Technol. 47 (2013) 8724–8732.

[42] S. Rtimi, D.D. Dionysiou, S.C. Pillai, J. Kiwi, Advances in catalytic/photocatalytic bacterial inactivation by nano Ag and Cu coated surfaces and medical devices, Appl. Catal. B 240 (2019) 291–318.

[43] X. Chen, Z. Chen, C.Y. Lin, R. Chen, P. Huang, Y. Jin, Water disinfection by the UVA/electro-Fenton process under near neutral conditions: Performance and mechanisms, Chemosphere 308 (2022), 136488.

[44] Z. Yan, Z. Dai, W. Zheng, Z. Lei, J. Qiu, W. Kuang, W. Huang, C. Feng, Facile ammonium oxidation to nitrogen gas in acid wastewater by in situ photogenerated chlorine radicals, Water Res 205 (2021), 117678.

[45] Y. Jin, P. Huang, X. Chen, L.P. Li, C.Y. Lin, X. Chen, R. Ding, J. Liu, R. Chen, Ciprofloxacin degradation performances and mechanisms by the heterogeneous electro-Fenton with flocculated fermentation biochar, Environ. Pollut. 324 (2023), 121425.

[46] J. Yan, J. Peng, L. Lai, F. Ji, Y. Zhang, B. Lai, Q. Chen, G. Yao, X. Chen, L. Song, Activation CuFe₂O₄ by Hydroxylamine for Oxidation of Antibiotic Sulfamethoxazole, Environ. Sci. Technol. 52 (2018) 14302–14310.

[47] A. Georgi, A. Schierz, U. Trommler, C.P. Horwitz, T.J. Collins, F.D. Kopinke, Humic acid modified Fenton reagent for enhancement of the working pH range, Appl. Catal. B 72 (2007) 26–36.

[48] A.R. Lado Ribeiro, N.F.F. Moreira, G. Li Puma, A.M.T. Silva, Impact of water matrix on the removal of micropollutants by advanced oxidation technologies, Chem. Eng. J. 363 (2019) 155–173.

[49] J. Du, Z. Xu, H. Li, H. Yang, S. Xu, J. Wang, Y. Jia, S. Ma, S. Zhan, Ag_3PO_4/g-C_3N_4 Z-scheme composites with enhanced visible-light-driven disinfection and organic pollutants degradation: Uncovering the mechanism, Appl. Surf. Sci. 541 (2021), 148487.

[50] Y. Jin, S. Chen, P. Huang, X. Chen, C.-Y. Lin, L.-P. Li, X. Chen, R. Ding, J. Liu, R. Chen, Efficient water disinfection with ball milled Mg-biochar: The key role of trace Cu, Chin. Chem. Lett. (2023), https://doi.org/10.1016/j.cclet.2023.108444.

[51] X. Ke, T. Wei, G. Wei, A. Chen, X. Cheng, Z. Li, Z. Qin, Z. Pang, J. Pan, Y. Chen, C. Wei, X. Guan, X. He, G. Qiu, H. Wu, C. Wei, Integrated process for zero discharge of coking wastewater: A hierarchical cycle-based innnovation, Chem. Eng. J. 457 (2023), 141257.

[52] Y. Du, H. Chen, Y. Zhang, Y. Chang, Photodegradation of gallic acid under UV irradiation: insights regarding the pH effect on direct photolysis and the ROS oxidation-sensitized process of DOM, Chemosphere 99 (2014) 254–260.